Composite wedge failure using photogrammetric measurements and DFN-DEM modelling

Viviana Bonilla-Sierra, Marc Elmouttie, Frédéric-Victor Donzé, Luc Scholtes

▶ **To cite this version:**

Viviana Bonilla-Sierra, Marc Elmouttie, Frédéric-Victor Donzé, Luc Scholtes. Composite wedge failure using photogrammetric measurements and DFN-DEM modelling. Journal of Rock Mechanics and Geotechnical Engineering, 2017, 9 (1), pp.41-53. 10.1016/j.jrmge.2016.08.005 . hal-02963780

HAL Id: hal-02963780
https://hal.science/hal-02963780

Submitted on 15 Oct 2020

HAL is a multi-disciplinary open access archive for the deposit and dissemination of scientific research documents, whether they are published or not. The documents may come from teaching and research institutions in France or abroad, or from public or private research centers.

L'archive ouverte pluridisciplinaire **HAL**, est destinée au dépôt et à la diffusion de documents scientifiques de niveau recherche, publiés ou non, émanant des établissements d'enseignement et de recherche français ou étrangers, des laboratoires publics ou privés.

Distributed under a Creative Commons Attribution - NoDerivatives 4.0 International License

Journal of Rock Mechanics and Geotechnical Engineering 9 (2017) 41–53

Contents lists available at ScienceDirect

Journal of Rock Mechanics and Geotechnical Engineering

journal homepage: www.rockgeotech.org

Full Length Article

Composite wedge failure using photogrammetric measurements and DFN-DEM modelling

Viviana Bonilla-Sierra [a,b], Marc Elmouttie [c], Frédéric-Victor Donzé [a,*], Luc Scholtès [d]

[a] Université Grenoble Alpes/CNRS, UMR 5521 3SR, Grenoble, 38000, France
[b] IMSRN, Parc Pré Millet – 680 Rue Aristide Bergès, Montbonnot, 38330, France
[c] CSIRO Energy Flagship, Po Box 883, Pullenvale, QLD, 4069, Australia
[d] GeoRessources Lab., Université de Lorraine, CNRS, CREGU, Vandoeuvre-lès-Nancy, 54500, France

ARTICLE INFO

Article history:
Received 3 May 2016
Received in revised form
6 July 2016
Accepted 22 August 2016
Available online 7 December 2016

Keywords:
Open pit mine
Polyhedral modelling
Discrete fracture network (DFN
Discrete element method (DEM)
Wedge failure

ABSTRACT

Analysis and prediction of structural instabilities in open pit mines are an important design and operational consideration for ensuring safety and productivity of the operation. Unstable wedges and blocks occurring at the surface of the pit walls may be identified through three-dimensional (3D) image analysis combined with the discrete fracture network (DFN) approach. Kinematic analysis based on polyhedral modelling can be used for first pass analysis but cannot capture composite failure mechanisms involving both structurally controlled and rock mass progressive failures. A methodology is proposed in this paper to overcome such limitations by coupling DFN models with geomechanical simulations based on the discrete element method (DEM). Further, high resolution photogrammetric data are used to identify valid model scenarios. An identified wedge failure that occurred in an Australian coal mine is used to validate the methodology. In this particular case, the failure surface was induced as a result of the rock mass progressive failure that developed from the toe of the structure inside the intact rock matrix. Analysis has been undertaken to determine in what scenarios the measured and predicted failure surfaces can be used to calibrate strength parameters in the model.

© 2017 Institute of Rock and Soil Mechanics, Chinese Academy of Sciences. Production and hosting by Elsevier B.V. This is an open access article under the CC BY-NC-ND license (http://creativecommons.org/licenses/by-nc-nd/4.0/).

1. Introduction

Assessment of unstable wedges and blocks occurring at proposed and operational surface mine excavations is critical for risk management in open pit mining. Discrete fracture networks (DFNs) are being increasingly used in the mining and civil engineering communities for analysis of in-situ rock mass fragmentation as defined by the presence of individual rock blocks (e.g. Wang et al., 2003; Rogers et al., 2007; Elmouttie and Poropat, 2012). The DFN approach combined with polyhedral modelling and kinematic analysis has been proven useful in providing a first pass and rapid assessment of both the location and likelihood of these potential hazards. This is due to the relatively low computational costs associated with this method supporting probabilistic approaches and multiple modelling scenarios (Elmouttie and Poropat, 2014). However, the method does not account for composite failure mechanisms involving both structurally controlled and rock mass progressive failures.

A complementary approach which consists in coupling DFN with geomechanical modelling, such as the discrete element method (DEM), provides the capability to simulate composite failure mechanisms. The pertinence of this approach has been previously demonstrated by studying failures in natural rock slopes involving progressive failure mechanisms (Bonilla-Sierra et al., 2015a). In particular, the DEM-DFN approach enables to simulate the spatiotemporal evolution of the micro-cracking occurring within the intact rock as well as the creation of critical failure surfaces through the coalescence of both induced and pre-existing fractures (Harthong et al., 2012; Scholtès and Donzé, 2012; Bonilla-Sierra et al., 2015b). The model output can be analysed to identify the development of critical failure surfaces and to estimate the kinematics of the failure.

The DEM has been used extensively in the analysis of rock slope instabilities due to its high capability to simulate fracture initiation and propagation (Stead et al., 2001). For instance, Eberhardt et al. (2004) and Eberhardt (2008) were among the first to present

* Corresponding author.
E-mail address: frederic.donze@3sr-grenoble.fr (F.-V. Donzé).
Peer review under responsibility of Institute of Rock and Soil Mechanics, Chinese Academy of Sciences.

http://dx.doi.org/10.1016/j.jrmge.2016.08.005
1674-7755 © 2017 Institute of Rock and Soil Mechanics, Chinese Academy of Sciences. Production and hosting by Elsevier B.V. This is an open access article under the CC BY-NC-ND license (http://creativecommons.org/licenses/by-nc-nd/4.0/).

discontinuum modelling of massive failures in natural rock slopes, focussing more specifically on the significance of rock bridges failure on the overall slope behaviour. The kinematic mechanisms and fracture propagation in large open pit mines were also investigated (Elmo et al., 2009), assessing the reliability of standard slope stability analysis methods in two (2D) and three dimensions (3D). Later on, combined remote sensing techniques were coupled with 3D discrete element analysis to assess the instabilities of a quarry in Italy (Francioni et al., 2014), presenting and discussing the advantages and disadvantages of using realistic 3D surfaces coupled to a 3D geomechanical model.

In this paper, the main objective tries to use the DFN-DEM approach as a tool to gain insights into validating candidate structural models for a case study dealing with composite failure processes (yielding along pre-existing structures and yielding of the rock matrix). DFN-DEM modelling was applied to studying the collapse of a wedge that occurred on an open pit wall in an Australian coal mine. The highwall of the coal mine was surveyed by the CSIRO using stereo photogrammetry although the process described in this paper is compatible with the use of any high resolution topographic data (e.g. laser). The wedge was first characterised geometrically using digital mapping and imported into the geomechanical model. The model was calibrated based upon the available data characterising the joints and the intact rock properties. Failure was then simulated and analysed from the original collapse case, testing two different types of rocks, one very weak and another one moderately strong, according to the classification by Hoek and Bray (1981). The simulated failure surfaces were then compared to the one obtained by the digital mapping in order to validate the predictions of these models.

For additional analysis, the original DFN was modified and even totally removed to assess the dependence of the failure mechanism on the structural model and on the mechanical properties of the rock mass.

2. Case study

A 3D image of the failure surface was first built from photogrammetric data acquisition performed after the wedge collapse (Elmouttie et al., 2012). Visible geological structures could be identified directly on the 3D image and mapped as polygonal surfaces (Fig. 1). The analysis of the failure surface led to the identification of two distinct joints as being responsible for the wedge formation. The beds on the wall are made up of conglomerates, breccias and pebbly sandstones to siltstones and the dominant material between the coal seams consists of coarse to fine sandstones (Elmouttie et al., 2012).

Close inspection of the 3D image revealed that this was not a simple wedge failure. Indeed, intact rock failure had occurred towards the bottom of the wedge as suggested by the difference in the rock surface appearance at this location (Fig. 2). Using a polyhedral model analysis, the presence of the unstable block was correctly identified but did not register as a hazard, since the wedge is kinematically constrained by its intact rock base due to the presence of a rock bridge. This example illustrates the limitations of polyhedral models to assess stability when composite failure mechanisms are involved (Elmouttie et al., 2012). In order to overcome this deficiency, a DFN-DEM modelling approach was thus carried out, focussing on this specific part of the wall.

The wall, mainly made up of sandstone, has been extensively characterised through laboratory tests (Elmouttie et al., 2012). The database provides the mechanical properties of a large quantity of samples taken in different zones of the wall, presenting a high variability in the mechanical properties between samples. Ideally, this variability can be represented in the modelling either deterministically (through the use of accurately defined domains) or, more likely through stochastic representation for rock mass properties. Given the computational demands of the DEM, an alternative approach was carried out here to study a limited number of scenarios.

In this work, the possibility of using the in-situ failure surface measured by high resolution photogrammetry in order to validate different failure scenarios was investigated. These scenarios involve the consideration of either the weakest sandstone or the strongest sandstone in the rock mass model. The laboratory-scale properties of both sandstones are listed in Table 1.

3. Structural model

Some geometric simplifications were performed to facilitate the modelling. In particular, the highwall and discontinuities were represented as planar surfaces. The volume used for the numerical model is constrained by the surface built using photogrammetric techniques (Fig. 3a). The DFN used for the post-failure analysis includes two polygonal surfaces whose orientations were assigned accordingly to the structural analysis (Fig. 1). Each surface represents a pre-existing discontinuity inside the rock mass. The one on the left has a dip angle of 85° and is oriented N23°W, and the one on the right has a dip angle of 45° and is oriented N113°E.

This DFN geometry assumes that the persistence of the two discontinuities is sufficiently large to create the hazardous wedge and to constrain its stability to the presence of the rock bridge at its

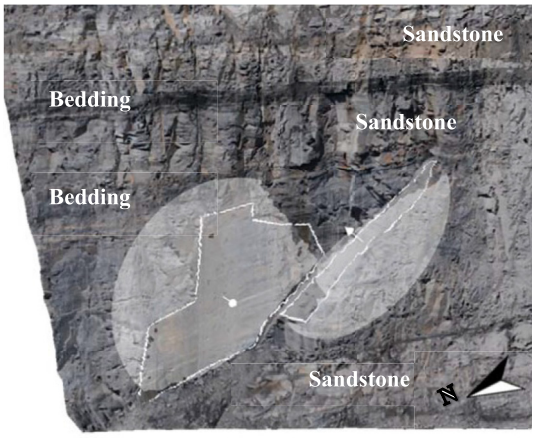

Fig. 1. Wedge failure in a highwall.

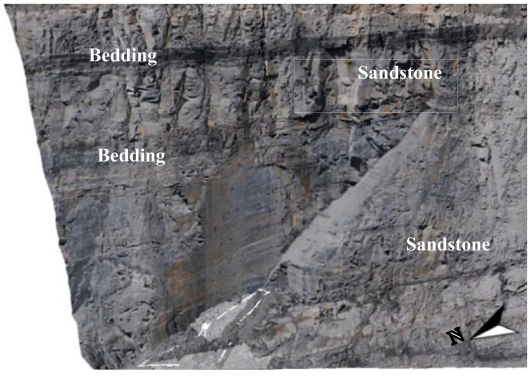

Fig. 2. Rock failure at the toe of the wedge outlined with a white polygon at the lower part of the figure.

Table 1
Laboratory-scale properties of the rock matrix for weak and strong sandstones.

Material	Density (kg/m^3)	Young's modulus, E (GPa)	Poisson's ratio, ν	Tensile strength, (MPa)	Uniaxial compressive strength (UCS) (MPa)
Weak sandstone	1900	3	0.3	1	8
Strong sandstone	2300	10	0.2	5	50

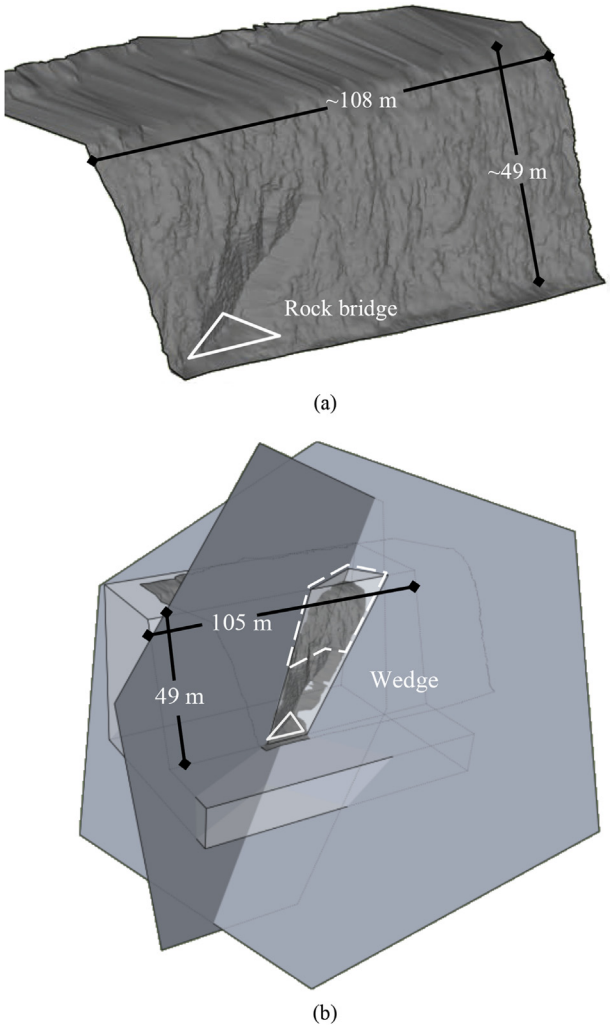

Fig. 3. 3D geometric model and associated DFN used for the numerical simulations. (a) The surface of the wall built by photogrammetry and (b) the DFN and the volume used for simulations, merged with the surface of the wall, showing the constrained wedge (right). The idealised rock bridge is highlighted with the white triangle.

toe. This simplification neglects the presence of other geological structures, such as bedding planes, to focus the analysis on the failure of the rock bridge only. One consequence of this simplification is that heterogeneity in rock strength, both within the wedge and surrounding rock mass, is neglected and the observed fragmentation of the wedge (with part of the structure remaining in the highwall) has not been captured in the modelling process (Fig. 3b).

4. Numerical model

DEM was chosen in this study for its capability to model the progressive failure of the rock matrix (Donzé and Magnier, 1995; Potyondy and Cundall, 2004). The simulations were carried out using Yade Open DEM, an extendable open-source software for discrete numerical modelling (Kozicki and Donzé, 2008, 2009). The intact rock is represented by an assembly of bonded discrete elements (DEs, also referred as particles). Each inter-particle bond obeys elastic-brittle behaviour in both normal and tangential directions. Under external loading, the bonds can break either by tension or shear failure mechanisms following a modified Mohr-Coulomb criterion with a tensile cut off (see Scholtès and Donzé (2013) for details).

The micro-cracks resulting from bond breakage can coalesce one with another to form macro-fractures. The model was calibrated based upon the properties measured by point load index tests and uniaxial compressive tests carried out on-site. Usually, the rock mass strength is assumed to be considerably reduced as the sample size increases. According to Hoek and Brown (1980), the uniaxial compressive strength UCS_d of a rock specimen with a diameter of "d" in mm can be related to the uniaxial compressive strength UCS_{50} of a 50 mm diameter sample by the following relationship:

$$UCS_d = UCS_{50}\left(\frac{50}{d}\right)^{0.18} \quad (1)$$

Hence, this criterion was used to consider the reduction in strength related to the increase of the sample, i.e. from the laboratory-scale to the metre-scale. A scaling factor of 0.6 was consequently applied to the strength measured at the laboratory to consider the scale effect at the metre-scale. Consequently, the aforementioned UCS values of 8 MPa and 50 MPa were scaled to obtain the UCS_{1000} values of 5 MPa and 30 MPa for the weak and the strong sandstones, respectively. The properties of both sandstones are summarised in Table 2.

To reproduce the behaviour of these two sandstones, a calibration of the model was carried out to determine the related DEM parameters. The elastic properties and the strength of the simulated rock are determined by performing uniaxial tensile and compressive tests, as well as triaxial tests simulations.

In the present DEM model, the non-linearity of the failure envelope and the ratio between the tensile strength and the compressive strength of both types of sandstone are controlled by the number of interaction forces per DE (which controls the degree of interlocking, see Scholtès and Donzéfor (2013) for details), which can be set by defining a given interaction range coefficient that allows for near neighbour interaction. The larger this coefficient is, the larger the number of interaction forces and the more brittle the material are. On the contrary, if the coefficient is close to one, the simulated material presents a granular fabric and behaves as a weak rock.

The DEM parameters used to simulate the macroscopic responses of the weak and the strong sandstones are summarised in Table 3. Therefore, the mechanical properties determined at the laboratory-scale and at the macroscopic scale for the weak and strong sandstones presented in Tables 1 and 2, respectively, are consistent with the bond-scale values shown in Table 3. The stress–strain curves obtained by uniaxial tensile and compressive tests simulations are plotted in Fig. 4 for both types of sandstone. The predicted failure envelopes for weak and strong sandstones and the related stress–strain curves are presented in Fig. 5. A linear fit between the axial stress and the confining stress allows for the estimation of the corresponding friction angle of the rock material (Hoek and Brown, 1997).

No experimental data were available for the joint properties. The joint surfaces were described on-site as clay-coated and weak with significant oxidation. A friction angle of 20° was then assumed

Table 2
Macroscopic properties of the rock matrix for weak and strong sandstones.

Material	Volumetric mass density (kg/m^3)	Young's modulus, E (GPa)	Poisson's ratio, ν	Tensile strength (MPa)	UCS (MPa)	Cohesion (MPa)	Friction angle (°)
Weak sandstone	1900	3	0.3	0.6	5	1.4	31.1
Strong sandstone	2300	10	0.2	3	30	6.4	42.5

Table 3
Bond-scale properties of the rock matrix for weak and strong sandstones. $\overline{D}$ is the harmonic mean of the interacting particles diameters (Scholtès and Donzéfor, 2013). Here, $\overline{D} = 0.88$ m.

Material	DE density (kg/m^3)	Bond normal stiffness (GPa m)	Bond shear/normal stiffness ratio	Bond tensile strength (MPa)	Bond cohesion (MPa)	Bond friction angle (°)	Number of contacts per DE	Interaction range coefficient
Weak sandstone	3390	$6\overline{D}$	0.45	1	8	13	8	1.02
Strong sandstone	4110	$18\overline{D}$	0.35	3.8	38	15	10	1.13

in the model. Such an assumption was deemed acceptable given the goals of this research were to demonstrate the use of high resolution failure surface data to validate model selection. However, discontinuity surface properties can represent a significant source of uncertainty in the geomechanical modelling process.

Discontinuities are explicitly included in the DEM model by using the smooth joint model (SJM) which ensures a constitutive mechanical behaviour of the discontinuities (Cundall et al., 2008; Mas-Ivars et al., 2011; Scholtès and Donzé, 2012). The SJM formulation consists in reorienting each inter-particle interaction intersecting the discontinuity plane, according to its surface orientation, in order to avoid the dependence of the behaviour on the model discretisation and on the DE shape (see Scholtès and Donzé (2012) for details). The joint behaviour was calibrated through direct shear tests simulations. The stress–strain curves obtained for constant normal loads σ_n ranging from 0.25 MPa to 1.5 MPa are shown in Fig. 6 along with the associated failure envelope. The SJM formulation ensures a direct equivalence between the macroscopic properties and the bond-scale properties. Therefore, a calibrated inter-particle friction angle equal to 20° leads to a macroscopic friction angle of 20°.

5. Strength reduction method

In the presence of rock bridges, the slope model can remain stable after the application of initial stress conditions induced by gravity loading. In this case, a strength reduction method, i.e. the tensile and shear strength reduction (TSSR) method, was performed to trigger failure (Bonilla-Sierra et al., 2015a,b). The TSSR method involves the progressive and simultaneous decreases of both the tensile strength and the cohesion of the inter-particle bonds making up the rock matrix while the properties of the joints remain unchanged. Acting at the particle scale, the TSSR method contributes to decreasing progressively the macroscopic tensile and compressive strengths of the simulated rock material.

TSSR is used here to simulate the progressive degradation process. The method has been successfully applied in previous works using DEM (Scholtès and Donzé, 2012, 2015). The interest of the TSSR method is that it involves the progressive decrease of the inter-particle bond strength by reducing simultaneously both their tensile and shear components. The result of this local strength reduction is the reduction of the global strength of the material and the possibility for micro-cracks to develop in places where the stresses concentrate. Although being an oversimplification of the actual degradation process taking place in nature, the method presents the advantage of keeping the same shape for the failure envelope of the rock material during the degradation process, ensuring therefore a realistic behaviour. In addition, keeping record of the value of the reduction factor applied at the bond-scale, it is possible to evaluate the strength properties of the material at failure. The TSSR method is controlled through the introduction of a TSSR factor, which is applied iteratively to the initial bond strength, until failure occurs (Bonilla-Sierra et al., 2015a).

Eventually, as a result of this degradation process, failure occurs at locations where the material is no longer able to sustain the loading. The progressive failure of the rock mass can be tracked by monitoring the spatiotemporal distribution of the micro-cracks that appear as the material strength decreases. Finally, a failure surface can be determined from the location of the micro-cracks inside the model.

In this study, the slope model was first stabilised by applying gravity in order to initialise the in-situ stress conditions. It is necessary to adjust the volumetric mass density from the macroscopic scale to the particle scale (see Tables 2 and 3), based on the difference in porosity between the real rock and the DE assembly, in order to ensure an equivalent stress field inside the model. After stabilisation, the rock matrix strength was then gradually reduced by iteratively applying the TSSR method every 1000 iterations until failure occurred. The strength reduction is applied every 1000 iterations because through experience, it had been observed that during this period, the model may recover its stability in a conservative manner and a new strength reduction can be applied. In any case, strength reduction is performed only if the model is stabilised by checking the amount of particles having a velocity higher than the predefined threshold discussed below.

The strength reduction factor is defined as follows (Bonilla-Sierra et al., 2015a):

$$\mathrm{TSSR} = \frac{\text{Current strength}}{\text{Initial strength}} \tag{2}$$

The TSSR factor is decreased iteratively until an unstable DE volume is detected in the model. This unstable volume is calculated at each iteration step and is defined as the volume of particles experiencing a velocity higher than 1 cm/s. This threshold was chosen after applying the TSSR factor to several cases with similar discretisation since the destabilisation was irreversible once the velocity of the DE exceeds this value. Defining V_p as the volume of a particle, the quantity of $1000V_p$, which is around 10% of the volume of the wedge, was chosen as the threshold value for characterising slope failure. This threshold choice is the result of previous simulations run in a similar scale, i.e. similar DE size (Bonilla-Sierra et al., 2015a,b), in which the value of 1 cm/s had shown to represent a reliable stability indicator. When the volume of particles with velocity higher than 1 cm/s is greater than this threshold, failure is said to occur and the TSSR is no longer applied.

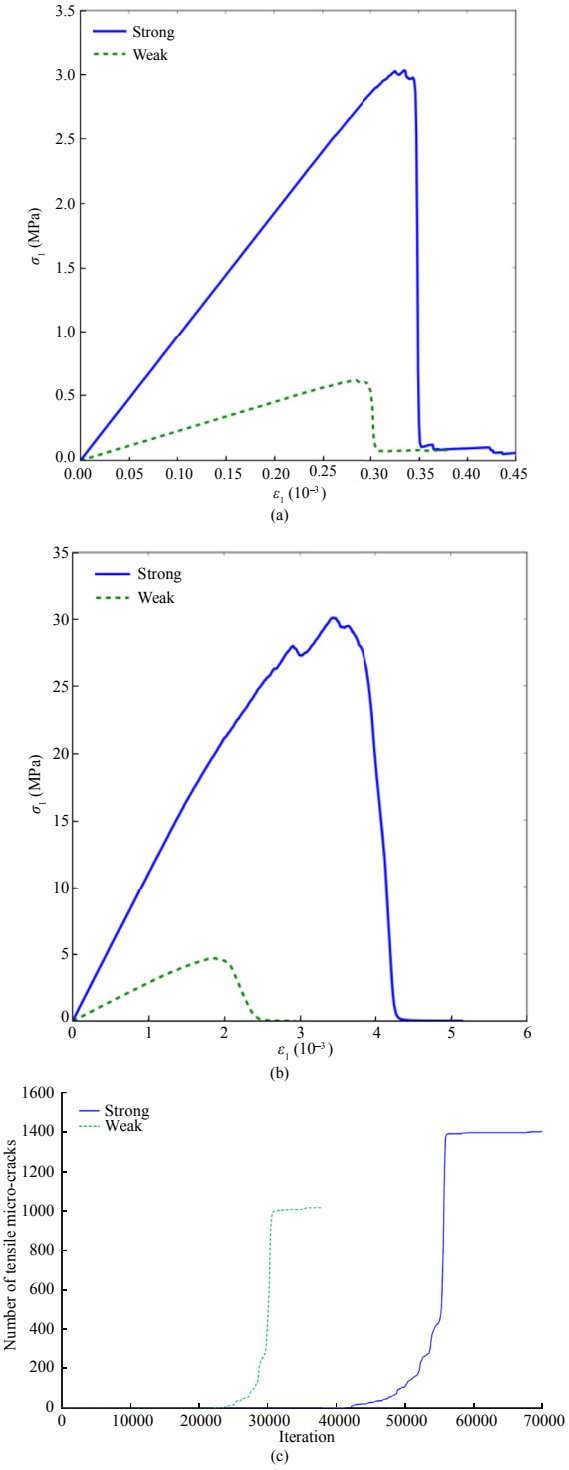

Fig. 4. (a) Stress–strain curves obtained from uniaxial tensile and (b) compressive test simulations performed on the rock matrix for the average and maximum values calibrated to the weak and the strong sandstones, respectively. (c) Evolution of the amount of micro-cracks during the tensile tests.

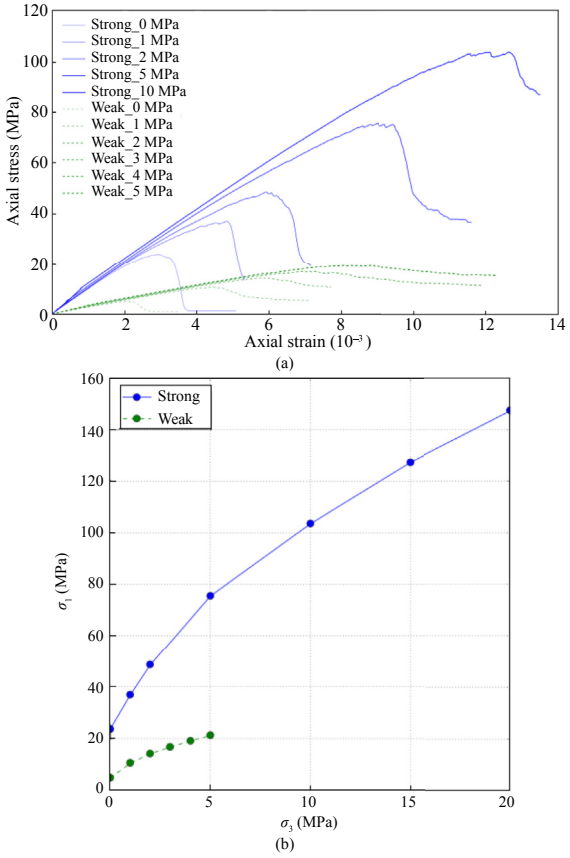

Fig. 5. (a) Stress–strain curves obtained from triaxial tests with the corresponding confining stress given on the top left corner, and (b) the predicted failure envelopes for the strong and weak sandstones.

6. Results

6.1. Stability analysis

In Fig. 7, the evolutions of the unstable volume and of the strength reduction factor are plotted as a function of the simulation time, for both types of sandstone. Before the TSSR factor was applied, the system went through a stabilisation phase under the application of the gravity force. Once the entire volume was stabilised, i.e. the unstable volume was nil, the TSSR was then iteratively applied until failure occurred (black curve in Fig. 7). Before failure, indicated by a vertical black dashed line in Fig. 7, the slope destabilised basically each time the TSSR was applied. However, the model reached a new equilibrium state before the next strength degradation was applied.

In parallel, the amount of micro-cracks occurring during the simulation was recorded. As soon as the rock strength was reduced to 3.2% and 23.7% of their initial values for the strong and weak sandstones, respectively, the number of micro-cracks located at the toe of the wedge started to increase dramatically and kept increasing as failure occurred (Figs. 8 and 9). For both types of sandstone, notwithstanding the differences in their strengths, the location of the initial fracturing pattern was in a good qualitative agreement with the observation made in field.

As shown in Figs. 10 and 11, failure developed as a result of the coalescence of micro-cracks propagating upward from the toe of the wedge in both cases, with a larger process zone for the strong sandstone because of the greater interlocking effect. The number of micro-cracks was also higher in the strong sandstone model than that in the weak sandstone model, due to the higher density of initial cohesive bonds. As a consequence, micro-cracks started to appear at the front part of the wall surrounding the wedge. The initiation and further propagation of the micro-cracks at the toe of the wedge triggered the destabilisation of the whole block.

As expected, the total unstable volume corresponds to the entire wedge volume, which is around 3200 m^3, as observed in the lower right of Figs. 10 and 11.

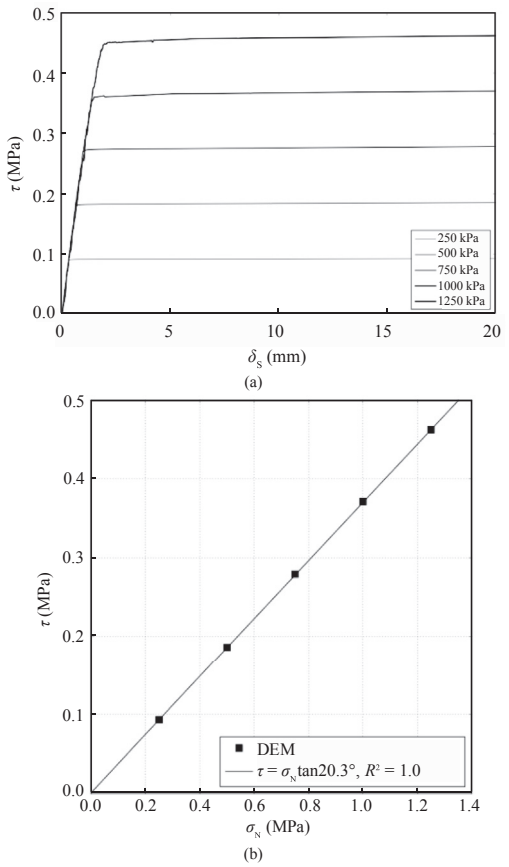

Fig. 6. (a) Stress–strain curves obtained from direct shear tests performed on the calibrated model under a constant normal load σ_N ranging from 0.25 MPa to 1.25 MPa, where τ is the shear stress and δ_S is the shear displacement of the joint; and (b) the corresponding predicted failure envelope for the rock joint.

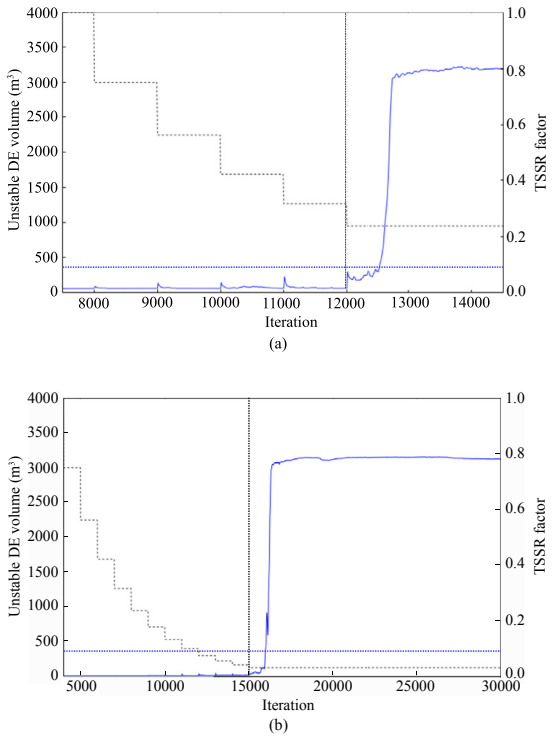

Fig. 7. The TSSR factor (black dashed curve) and the evolution of the unstable volume (blue continuous curve) as a function of the iteration numbers for the weak sandstone (a) and strong sandstone (b). The threshold volume is shown with the horizontal blue dashed line. The vertical black dashed line delimits the iteration at which failure occurred.

The failure mechanisms driving the destabilisation of the wedge seem to be comparable for both weak and strong sandstones. To highlight the similarity in the failure pattern for both, a side view of the velocity field is plotted after failure in Fig. 12, showing the wedge sliding towards its base.

6.2. Failure surface identification

In the DFN-DEM model, macro-fractures result from the coalescence of micro-cracks (Scholtès and Donzé, 2015). The micro-cracks located at the toe of the wedge were thus isolated in order to identify the failure surface (Fig. 13). As mentioned in the previous section, the number of micro-cracks is lower in the weak sandstone model. The consequence is a difference in the density of the micro-cracks at the toe of the slope for each case. Nevertheless, the localisation of the failure surface was very similar for both cases (Fig. 13).

The micro-cracks form a point cloud whose convex hull can be computed using any mesh-processing software. The convex hull is defined as the boundary of the minimal convex shape that contains the given set of points. In 3D, the convex hull is a convex polyhedron (de Berg et al., 2008). The polyhedron can then be meshed using triangulation techniques over its constitutive points.

From the resulting volume, the failure surfaces for both weak and strong sandstones could thus be extracted as the lower boundary of the polyhedron. Since the numerical model was created within the same geo-referencing system used to generate the 3D image, the failure surfaces extracted from the numerical simulations could be directly superimposed on the original failure surface measured using photogrammetry. As observed in Fig. 14, a good qualitative agreement is found between the numerical predictions and the actual failure surface.

For further analysis, a quantitative comparison between the simulated and observed failure surfaces was performed by calculating the minimum distances between the simulated micro-crack locations and the best-fit plane to the failure surface (Table 4). Despite a quantitative agreement, a discrepancy arises in the dip direction of the simulated data. This discrepancy can be observed in Fig. 15, where the generated micro-cracks (in red) are superposed over the location of the actual failure surface, represented by its contour (in blue). We attribute this to the relatively sparse point cloud used to fit the failure surface in the model. This difference might be reduced by increasing the density of the DE assembly used in the simulations. Both modelled scenarios were found to be consistent to the high resolution photogrammetric data of the failure surface. The final unstable volume was similar for both sandstones, and was equal to the total volume of the wedge constrained by the discontinuities. Qualitatively, it was observed that the failure mechanism was controlled by the geological structures considered in the model rather than by the mechanical properties of the rock. Note that the local strength (i.e. at the bond-scale) at failure was different in each case. The local strength of the strong sandstone had to be reduced up to 3.2% of its initial value in order to trigger failure, which is around eight times lower than the TSSR factor needed to destabilise the wedge in the case of the weak sandstone model. For instance, at the bond-scale, the final local tensile strength for the weak sandstone was 0.24 MPa and the final local cohesion was 1.92 MPa, which correspond to a reduction of 23.7% of their initial values. For the strong sandstone, the final local

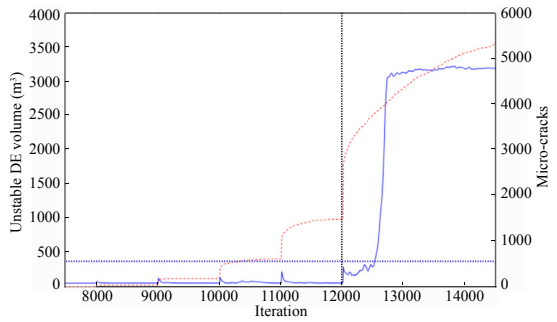

Fig. 8. For the weak sandstone, the evolution of the unstable volume (blue continuous curve) and the cumulative amount of micro-cracks (red dashed curve) as a function of the iteration numbers. The threshold volume is shown with the horizontal blue dashed line. The vertical black dashed line delimits the iteration at which failure occurred.

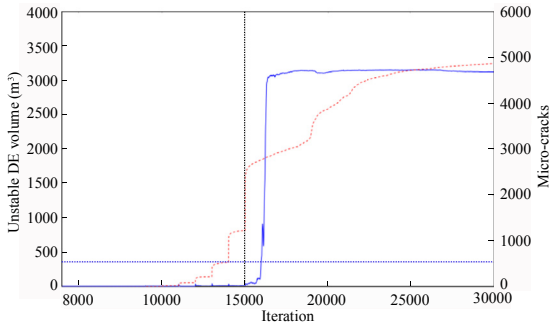

Fig. 9. For the strong sandstone, the evolution of the unstable volume (blue continuous curve) and the cumulative amount of micro-cracks (red dashed curve) as a function of the iteration numbers. The threshold volume is shown with the horizontal blue dashed line. The vertical black dashed line delimits the iteration at which failure occurred.

tensile strength was 0.12 MPa and the final local cohesion was 1.2 MPa. These differences at the bond-scale can be explained by the difference in the degree of interlocking between the two types of rock; more contacts per DE lead to higher decrease in their strength in order to reach the critical state.

We can therefore confirm that, given the model assumptions and simplifications used in this study, the weak sandstone model seems to provide consistent results with the weathered rock strength properties identified in the field.

7. Influence of the rock bridge size

The detachment of the wedge resulted from stress concentration at the toe of the wedge, where the rock bridge was located. In this particular case, the failure mechanism and the associated unstable volume seem to be strongly controlled by the geometry of the discontinuities that constrain the rock bridge to a reduced area located at the toe of the wedge. To investigate the contribution of the DFN to the failure surface geometry, different configurations were simulated.

7.1. The modified structural model

In the original case study, the area at the toe is estimated to be only 2.5% of the total surface area of the wedge, highlighted in red in Fig. 16a. In this particular case, it has been observed that the failure mechanism and the unstable volume were likely controlled by the DFN configuration rather than by the rock properties. By considering a different structural model, and therefore a larger area for the rock bridge, a different mechanical response may be expected. To do so, the DFN was pushed back inside the slope so as to increase the area of the rock bridge to 9% of the total surface area of the wedge as observed in Fig. 16b. The dip and dip direction of the discontinuities were kept unchanged.

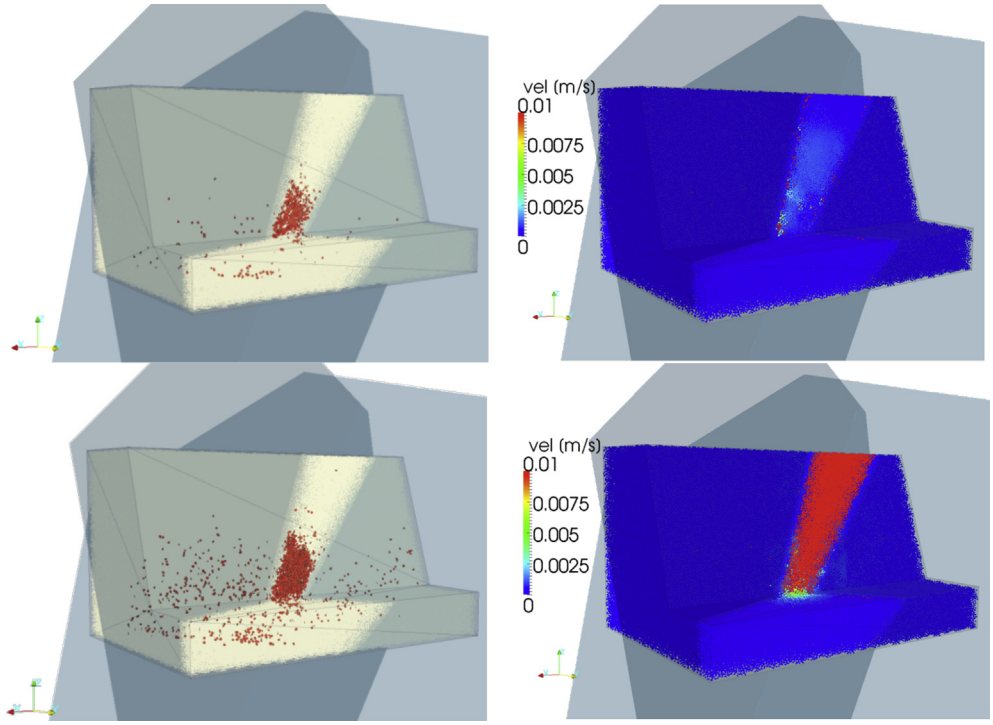

Fig. 10. 3D view of the weak sandstone model. On the top, the micro-cracks (left) and the velocity field (right) at 12,000 iterations. On the bottom, the micro-cracks (left) and the velocity field (right) at 13,000 iterations.

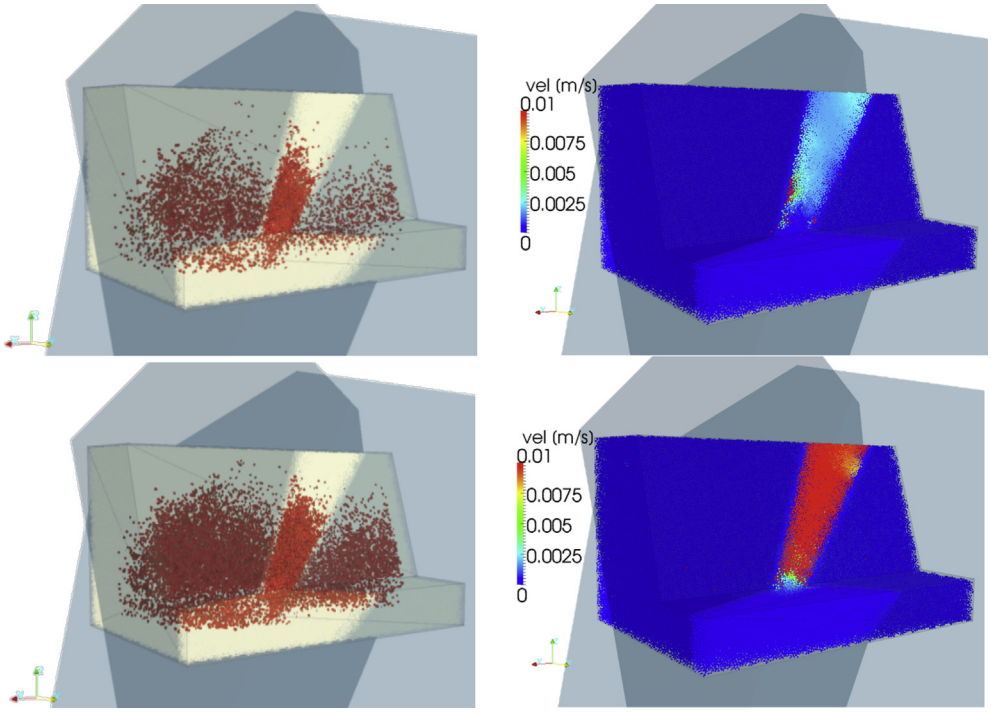

Fig. 11. 3D view of the strong sandstone model. On the top, the micro-cracks (left) and the velocity field (right) at 15,000 iterations. On the bottom, the micro-cracks (left) and the velocity field (right) at 16,000 iterations.

7.2. Failure mechanism

Simulations were run using the modified DFN for both strong and weak sandstones and the results were compared with the original configuration described in previous sections. The same TSSR method was applied in order to trigger failure.

For both the weak and strong sandstones, the collapsing volume can be identified and located through the velocity field at failure. To visualise the failure mechanisms, a vertical cut of the velocity field is plotted for both sandstones (Fig. 17). Contrary to the original case study, the mechanical properties of the rock appeared to have here an effect on the failure mechanisms of the wedge. For the weak sandstone, a circular slip surface, typical of weak homogeneous slopes, can be distinguished (Fig. 17, top). This behaviour results from the mechanical properties of the simulated medium. Indeed, a small degree of interlocking (DE interaction radius equal to 1.02 m) and a friction angle equal to 31.1° correspond to weathered rock masses or soil-like materials which are prone to circular failure (Wyllie and Mah, 2004). On the other hand, the strong sandstone has a larger degree of interlocking (DE interaction radius equal to 1.13 m) and a friction angle equal to 42.5° and clearly, the failure surface looks stepper and shallower than those in the case of the weak sandstone, as shown in Fig. 17 (bottom).

The influence of the mechanical properties of the rock material on the failure mechanisms was also investigated. It was shown that, although the structural features constrained the resulting unstable volume, they did not control the failure mechanism. The volume mobilised depends here on the strength of the sandstone. For the strong sandstone, the total volume of the wedge was partially destabilised, and its failure surface was shallower and steeper than those observed for the weak sandstone. For the latter, the entire volume of the wedge failed along a circular failure surface.

8. Stability of homogeneous rock masses

The importance of pre-existing structures was studied and it has been found that, depending on the size of the rock bridge, the failure mechanism and the mobilised volume may vary if the mechanical properties of the rock are modified. To conclude the analysis on the mechanical properties of the rock and their effect on

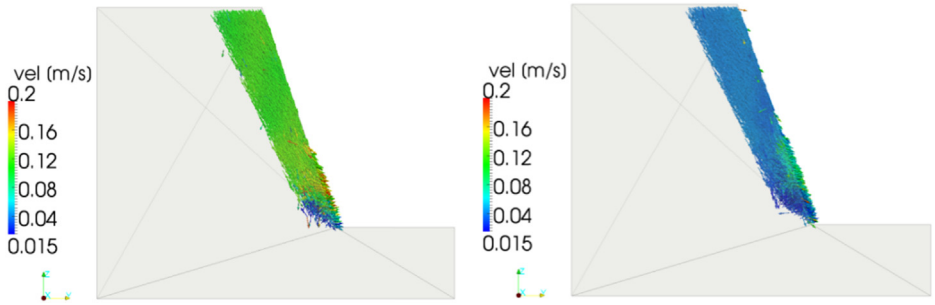

Fig. 12. Vertical cut of the velocity vector field plotted for the weak sandstone at 14,000 iterations (left) and for the strong sandstone at 17,000 iterations (right).

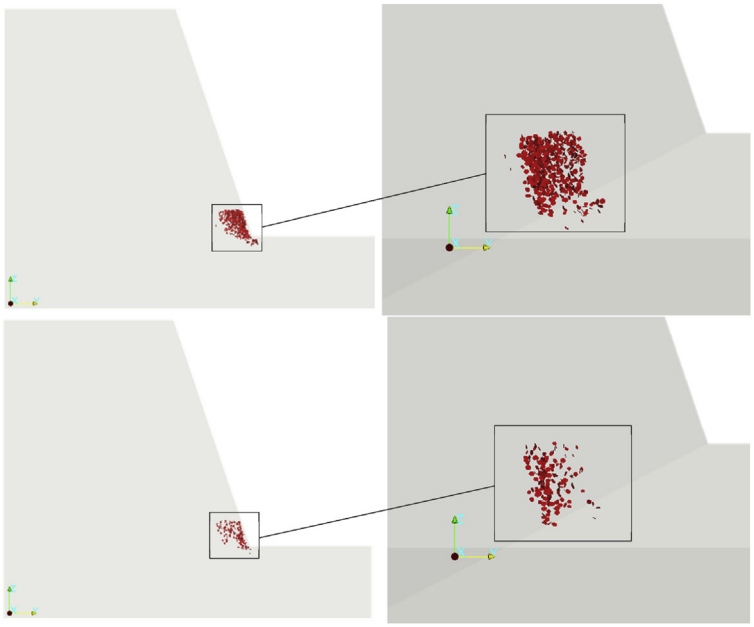

Fig. 13. Point cloud representing the micro-cracks appearing at the toe of the wedge for the strong sandstone after 14,000 iterations (top) and for the weak sandstone after 11,000 iterations (bottom).

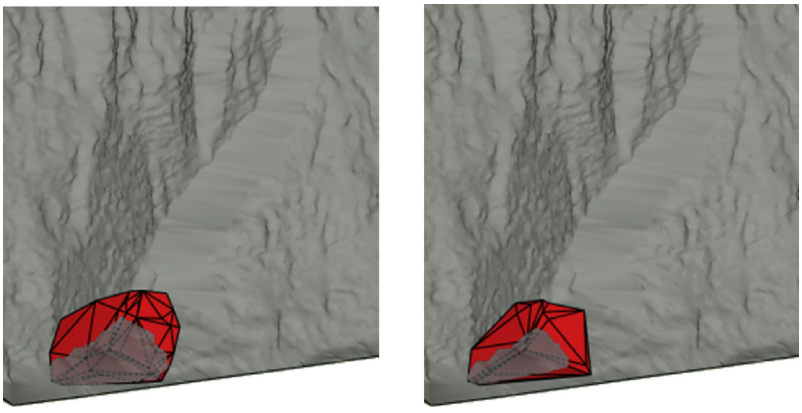

Fig. 14. Failure surface (in red) superposed to the highwall surface for the strong (left) and weak (right) sandstones.

rock slope stability, the DFN was removed in order to study the behaviour of the intact slope as a function of the nature of the rock material.

The TSSR method was applied in the same way as it was applied for the two previous cases. The unstable volume calculated at 3000 iterations after failure for the weak sandstone was around 6400 m^3 and tended to increase during the simulation. The velocity field at that moment of the simulation is shown in Fig. 18a. A curved failure surface can be identified from the vertical cut of the velocity field presented in Fig. 18b.

In comparison to the weak sandstone, the unstable volume recorded at 3000 iterations after failure for the strong sandstone was 3300 m^3, which is two times lower. In Fig. 19, the velocity field registered at that moment shows that the unstable volume for the strong sandstone was distributed at an equivalent height on the slope face as for the weak sandstone. Nevertheless, the depth of the failure surface is less important when the material strength is higher.

In the presence of pre-existing discontinuities, failure surface can be controlled by the location and the orientation of the

Table 4
Summary data comparing the simulated and observed failure surfaces.

Surface	Number of cracks in analysis	Best-fit-plane orientation (dip/dip direction ± 2°)	Exposed area of failure surface (±5 m^2) (m^2)	Average distance from simulated to observed surface (±1 m) (m)
Simulated surface (strong sandstone)	16	22°/011	46*	0.59
Simulated surface (weak sandstone)	9	24°/008	38*	0.36
Observed 3D surface	NA	30°/005	50	NA

Note: "*" means the values are calculated by projecting simulated failure surface onto observed best-fit plane and computing area of convex hull.

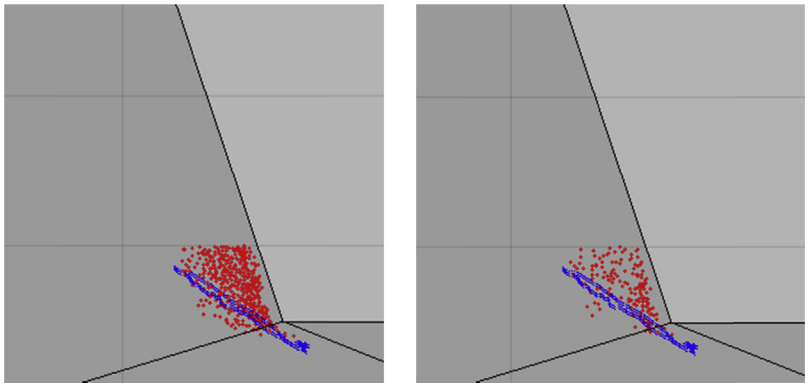

Fig. 15. Superposition between the simulated micro-cracks (in red) and the observed failure surface (point cloud in blue), for the strong (left) and weak (right) sandstones.

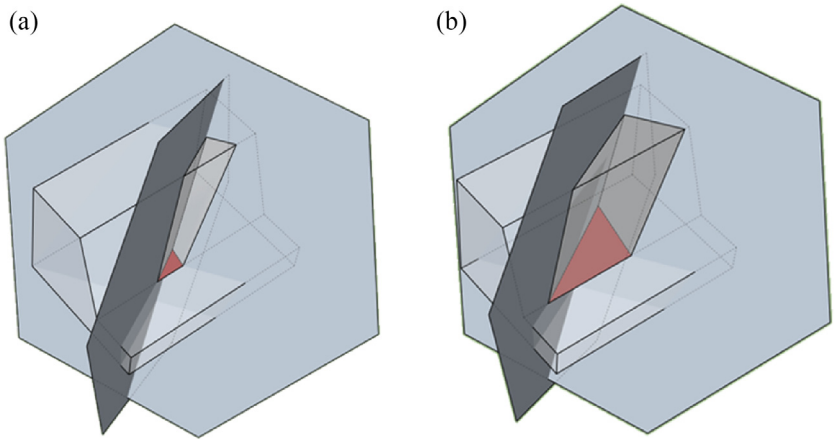

Fig. 16. Idealised rock bridge surfaces. (a) The original DFN with 2.5% of the total surface of the wedge as rock bridge and (b) the modified DFN with 9% of the total surface of the wedge as rock bridge.

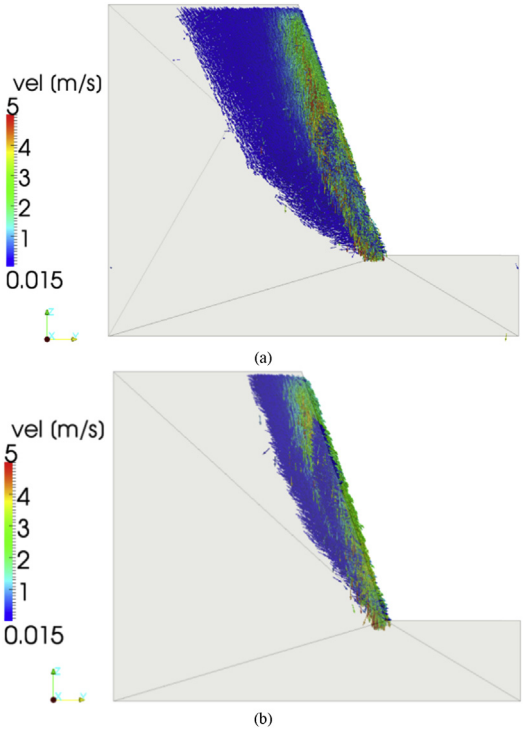

Fig. 17. Vertical cut of the velocity field plotted (a) for the weak sandstone at 31,000 iterations and (b) for the strong sandstone at 38,000 iterations.

geological features. Without discontinuities, only the material strength has an impact on the failure mechanism. For both types of sandstone, the unstable volume was homogeneously mobilised along a shallow circular surface, with differences in the depth and height depending on the mechanical properties of the rock. The failure observed for the weak sandstone presents a deep radius surface, in contrast with the shallow surface observed for the strong sandstone.

9. Discussion

In order to establish a qualitative understanding of the relative importance of the DFN geometry and material properties, the mechanical response of an open pit wall was studied under three different geometric scenarios, using two types of materials respectively calibrated to weak and strong sandstones. In the first scenario, the original DFN configuration constrained the rock bridge to a small area (2.5% of the total surface area of the wedge). In the second scenario, the DFN configuration was modified to increase the size of the rock bridge up to four times its original area. In the third scenario, the DFN was removed and the analysis was done focussing only on the influence of the mechanical properties of the rock matrix.

The ratio of the unstable volume to the total volume of the model (DE volume) is plotted in Fig. 20, as a function of the ratio between the rock bridge area and the total surface area of the wedge. When the rock bridge is small (original DFN), the entire

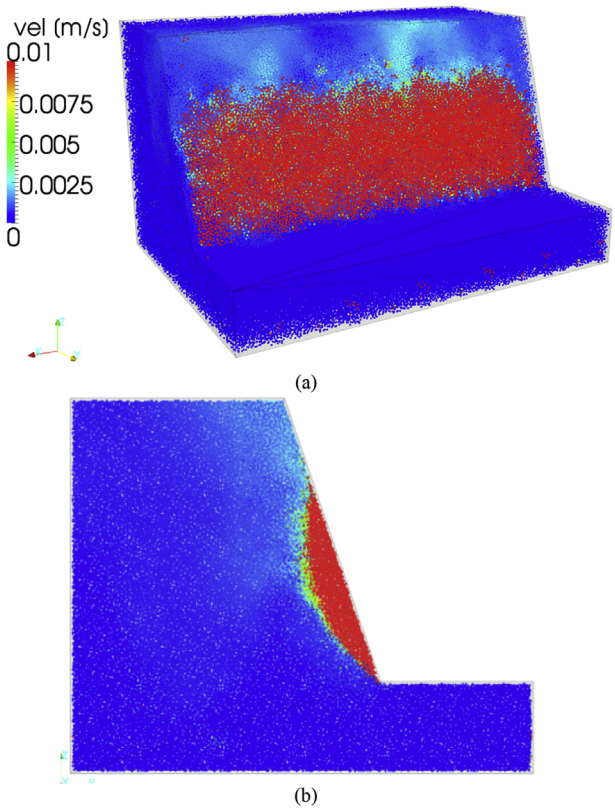

Fig. 18. Velocity field at 20,000 iterations for the weak sandstone: (a) 3D view and (b) centred vertical cut.

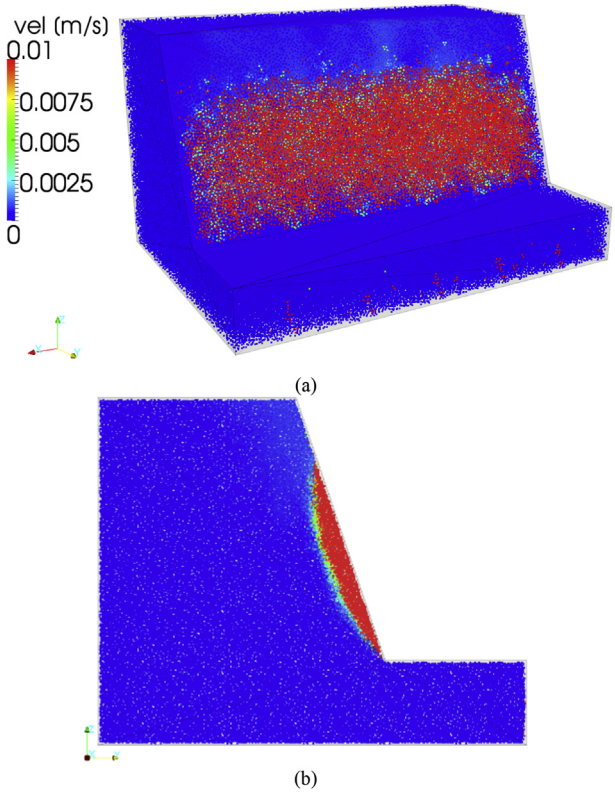

Fig. 19. Velocity field at 24,000 iterations for the strong sandstone: (a) 3D view and (b) centred vertical cut.

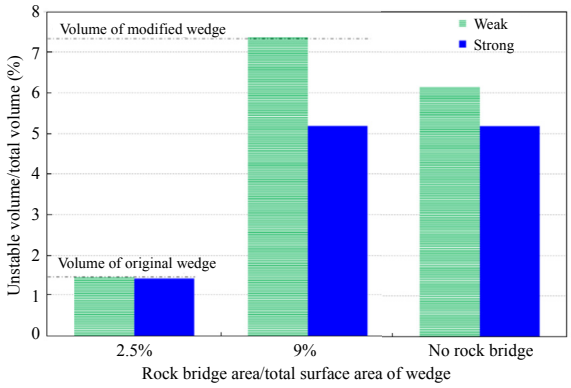

Fig. 20. Relationship between the unstable volume and the size of the rock bridge at the toe of the wedge.

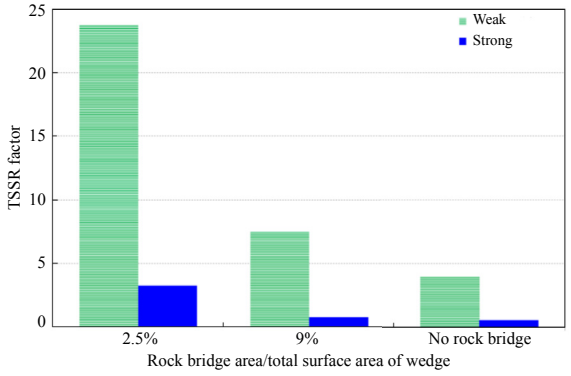

Fig. 21. Dependence of the TSSR factor at failure on the presence and size of the rock bridge at the toe of the wedge.

wedge is mobilised. When the rock bridge is larger or when there is no DFN, the mobilised volume is higher for the weak sandstone than that for the strong sandstone. However, in the case of the enlarged rock bridge, the mobilised volume is still constrained by the DFN, as 100% of the wedge volume collapsed for the weak sandstone, whereas 70% of the wedge collapsed for the strong sandstone. Due to the drastic strength reduction needed to trigger failure, areas surrounding the lower left part of the wedge were also destabilised. To summarise, the unstable volume is strongly controlled by the presence of the discontinuities that constrain the size of the rock bridge. As their configuration is modified, and the size of the rock bridge is increased, the material properties remain the predominant factor controlling the stability.

Regarding the TSSR factor, i.e. the strength reduction needed to trigger failure, the strength of the strong sandstone was reduced to lower values than the strength of the weak sandstone in all the cases. At the bond-scale, this is explained by the difference in the degree of interlocking between the two types of rock; more contacts per DE lead to higher decrease in their strength in order to reach the critical state. For both types of sandstone, the TSSR factor at failure decreases as the size of the rock bridge increases and it is similar to the factors obtained in the absence of DFN, as observed in Fig. 21. This can be explained by the fact that when the size of the rock bridge increases, the proportion of intact rock that assures the stability increases, and thus the rock strength has to be reduced to a lower value in order to destabilise the model. The decrease rate is also higher for the weak sandstone, indicating that

mechanically, this one is more affected by the presence of structural features.

10. Conclusions

The stability of an open pit highwall was assessed through numerical modelling. The study focused on a particular area of the wall where a wedge collapsed. A preliminary kinematic analysis based on polyhedral modelling showed that the wedge would remain stable due to the presence of a rock bridge at its base. DFN-DEM modelling was thus used for its capability to model the progressive failure of this kinematically constrained wedge.

Two types of sandstone were considered in the analysis, labelled respectively weak and strong, to include the high variability of the on-site characterisation. The geomechanical models were thus calibrated to either the weak or the strong sandstone in order to evaluate the effect of the mechanical properties on the failure process.

A strength reduction method, i.e. the TSSR method, was applied to simulating the progressive failure of the wedge. The coalescence of the micro-cracks propagating inside the model provided a simulated failure surface that was compared to the failure surface measured in the field through photogrammetric measurements. The difference of strength between the weak and strong sandstones showed no impact on the location or orientation of the simulated failure surface and both configurations were consistent with field measurements.

Furthermore, to investigate the effect of the mechanical properties of the rock on the failure mechanism and on the failure surface prediction, the DFN was modified in order to increase the size of the expected rock bridge. In this particular case, the coalescence of the micro-cracks could not provide a specific failure surface either for the weak sandstone or for the strong sandstone. The failure mechanism could be observed by assessing the unstable volume and the velocity field that showed differences in the way the wedge was mobilised depending on the strength of the material. In the case of the weak sandstone, a circular failure surface could be observed. For the strong sandstone, a shallow surface could be identified on the face of the wall. Moreover, it has been seen that the mechanical response of the weak sandstone was more affected than the strong one, in the presence of the structural features.

The proposed method has potential to validate modelling parameters such as rock strength or rock mass structure through comparisons between observed and predicted failure surfaces. A limiting factor of such approach lies in the limitation of the model resolution which can complicate comparison and interpretation of the simulated failure surface with the use of high resolution topographic data.

Conflict of interest

The authors wish to confirm that there are no known conflicts of interest associated with this publication and there has been no significant financial support for this work that could have influenced its outcome.

Acknowledgments

The authors are grateful to Philip Soole and Paul Maconochie for the acquisition of the photogrammetric data used in this study. The authors are also grateful to Nathan Ferdinands and Dave Edwards for providing site access and support at the mine. Brett Poulsen and Andy Wilkins are thanked for their fruitful discussions. This work has been supported by the IMSRN French Company through a CIFRE grant No. 2012/0710 and CSIRO Energy Flagship, QCAT in Australia. The laboratory 3SR is part of the LabEx Tec 21 (Investissements d'Avenir – grant agreement No. ANR-11-LABX-0030).

References

Bonilla-Sierra V, Scholtès L, Donzé FV, Elmouttie M. DEM analysis of rock bridges and the contribution to rock slope stability in the case of translational sliding failures. International Journal of Rock Mechanics and Mining Sciences 2015b;80:67–78.

Bonilla-Sierra V, Scholtès L, Donzé FV, Elmouttie MK. Rock slope stability analysis using photogrammetric data and DFN-DEM modelling. Acta Geotechnica 2015a;10(4):497–511.

Cundall PA, Pierce ME, Mas-Ivars D. Quantifying the size effect of rock mass strength. In: SHIRMS 2008, Proceedings of the 1st Southern Hemisphere International Rock Mechanics Symposium. Perth, Australia; 2008. p. 3–15.

de Berg M, Cheong O, van Kreveld M, Overmars M. Computational geometry: algorithms and applications. Springer; 2008.

Donzé FV, Magnier SA. Formulation of a 3D numerical model of brittle behaviour. Geophysical Journal International 1995;122(3):790–802.

Eberhardt E, Stead D, Coggan JS. Numerical analysis of initiation and progressive failure in natural rock slopes – the 1991 Randa rockslide. International Journal of Rock Mechanics and Mining Sciences 2004;41(1):69–87.

Eberhardt E. Twenty-ninth Canadian Geotechnical Colloquium: the role of advanced numerical methods and geotechnical field measurements in understanding complex deep-seated rock slope failure mechanisms. Canadian Geotechnical Journal 2008;45(4):484–510.

Elmo D, Moffitt K, D'Ambra S, Stead D. A quantitative characterisation of brittle rock fracture mechanisms in rock slope failures. In: International Symposium on Rock Slope Stability in Open Pit Mining and Civil Engineering, Santiago, Chile; 2009.

Elmouttie M, Poropat G, Soole P. Open cut mine wall stability analysis utilising discrete fracture networks. ACARP Final Report C20029 2012.

Elmouttie M, Poropat GV. A method to estimate in situ block size distribution. Rock Mechanics and Rock Engineering 2012;45(3):401–7.

Elmouttie M, Poropat GV. Quasi-stochastic analysis of uncertainty for modelling structurally controlled failures. Rock Mechanics and Rock Engineering 2014;47(2):519–34.

Francioni M, Salvini R, Stead D, Litrico S. A case study integrating remote sensing and distinct element analysis to quarry slope stability assessment in the Monte Altissimo area, Italy. Engineering Geology 2014;183:290–302.

Harthong B, Scholtès L, Donzé FV. Strength characterization of rock masses using a coupled DEM-DFN model. Geophysical Journal International 2012;191(2):467–80.

Hoek E, Bray JW. Rock slope engineering. 3rd ed. London: Institution of Mining and Metallurgy; 1981.

Hoek E, Brown ET. Practical estimates of rock mass strength. International Journal of Rock Mechanics and Mining Sciences 1997;34(8):1165–86.

Hoek E, Brown ET. Underground excavations in rock. London: Institution of Mining and Metallurgy; 1980.

Kozicki J, Donzé FV. A new open-source software developed for numerical simulations using discrete modeling methods. Computer Methods in Applied Mechanics and Engineering 2008;197(49–50):4429–43.

Kozicki J, Donzé FV. YADE-OPEN DEM: an open-source software using a discrete element method to simulate granular material. Engineering Computations 2009;26(7):786–805.

Mas-Ivars D, Pierce ME, Darcel C, Reyes–Montes J, Potyondy DO, Young RP, Cundall PA. The synthetic rock mass approach for jointed rock mass modelling. International Journal of Rock Mechanics and Mining Sciences 2011;48(2):219–44.

Potyondy DO, Cundall PA. A bonded-particle model for rock. International Journal of Rock Mechanics and Mining Sciences 2004;41(8):1329–64.

Rogers SF, Kennard DK, Dershowitz WS, van As A. Characterising the in situ fragmentation of a fractured rock mass using a discrete fracture network approach. In: Eberhardt E, Stead D, Morrison T, editors. Rock mechanics: meeting society's challenges and demands. London: Taylor & Francis Group; 2007. p. 137–44.

Scholtès L, Donzé FV. A DEM analysis of step-path failure in jointed rock slopes. Comptes Rendus Mécanique 2015;343(2):155–65.

Scholtès L, Donzé FV. A DEM model for soft and hard rocks: role of grain interlocking on strength. Journal of the Mechanics and Physics of Solids 2013;61(2):352–69.

Scholtès L, Donzé FV. Modelling progressive failure in fractured rock masses using a 3D discrete element method. International Journal of Rock Mechanics and Mining Sciences 2012;52:18–30.

Stead D, Eberhardt E, Coggan J, Benko B. Advanced numerical techniques in rock slope stability analysis – applications and limitations. In: International Conference on Landslides – Causes, Impacts and Countermeasures; 2001. p. 615–24.

Wang LG, Yamashita S, Sugimoto F, Pan C, Tan G. A methodology for predicting the in situ size and shape distribution of rock blocks. Rock Mechanics and Rock Engineering 2003;36(2):121–42.
Wyllie DC, Mah C. Rock slope engineering. CRC Press; 2004.

Dr. Viviana Bonilla-Sierra is a post-doctoral fellow in University Grenoble Alpes (France). She is currently studying the development of a twist fracture from a crack loaded in mode III using a 3D DEM. She is a civil engineer with 3 years of professional experience in project management in Colombia. She has obtained her M.S. degree in Geomechanics, Civil Engineering and Risk and her Ph.D. degree in Rock Mechanics, both from the Université Grenoble Alpes (France). She has built a solid background in photogrammetry and numerical modelling and their suitability for the analysis of rock slope stability. While being a doctoral student, she has collaborated with the CSIRO (Australia) geomechanics numerical modelling team to develop a method for coal mine highwall stability analysis, coupling DFN and DEM. Up to date, Dr. Bonilla-Sierra has published 2 peer-reviewed papers about rock slope stability analysis by using DEM modelling. She has participated in international geosciences conferences in Austria, Spain, Canada, Argentina and United States.